



Cite this: *Phys. Chem. Chem. Phys.*,
2019, 21, 22763

The effect of dimerization on the activation and conformational dynamics of adenosine A₁ receptor†

Yang Li,^a Mukuo Wang,^a Na Gao,^{ab} Dongmei Li*^a and Jianping Lin  *^{ab}

The adenosine A₁ receptor (A₁R) is one of four adenosine receptors in humans, which are involved in the function of the cardiovascular, respiratory and central nervous systems. Experimental results indicate that A₁R can form a homodimer and that the protomer–protomer interaction in the A₁R dimer is related to certain pharmacological characteristics of A₁R activation. In this work, we performed docking, metadynamics simulation, conventional molecular dynamics simulations, Gaussian-accelerated molecular dynamics simulations, potential of mean force calculations, dynamic cross-correlation motions analysis and community network analysis to study the binding mode of 5'-N-ethylcarboxamidoadenosine (NECA) to A₁R and the effect of dimerization on the activation of A₁R. Our results show that NECA binds to A₁R in a similar mode to adenosine in the A₁R crystal structure and NECA in the A_{2A}R crystal structure. The A₁R homodimer can be activated by one or two agonists with NECA occupying its orthosteric pockets in one (which we call the NECA–A₁R system) or both protomers (which we call the dNECA–A₁R system). In the NECA–A₁R system, activation is predicated in the protomer without NECA bound. In the dNECA–A₁R system, only one protomer achieves the active state. These findings suggest an asymmetrical activation mechanism of the homodimer and a negative cooperativity between the two protomers. We envision that our results may further facilitate the drug development of A₁R.

Received 20th July 2019,
Accepted 2nd October 2019

DOI: 10.1039/c9cp04060a

rsc.li/pccp

1. Introduction

G-protein-coupled receptors (GPCRs) are a large family of cellular signaling proteins on the cell surface that transmit extracellular signals, including hormones, pheromones and neurotransmitters, and trigger intracellular downstream signal transduction pathways that lead to cellular responses. GPCRs are involved in many human diseases, and thus are the targets of around 40% of all modern medicinal drugs.¹ Adenosine receptors (ARs) belong to the GPCR superfamily and mediate the physiological actions of nucleoside adenosine. There are four known types of ARs in humans, namely A₁R, A_{2A}R, A_{2B}R, and A₃R. Of these, A₁Rs are widely distributed throughout the entire body and regulate a variety of functions of the cardiovascular, respiratory, renal, inflammation and central nervous systems.^{2–5} Therefore, it is important to explore the detailed

molecular mechanism and the dynamic information of A₁R in response to agonist binding.

Over the past few years, there have been several docking and molecular dynamics (MD) simulation studies regarding the agonist or allosteric modulator interactions with A₁R.^{6–9} However, these studies were performed using an A₁R homology model based on the A_{2A}R crystal structure owing to the lack of an A₁R crystal structure. In 2017, Christopoulos and coworkers determined the first X-ray crystal structure of A₁R, which was covalently bound to an antagonist, DU172 (PDBID: 5UEN).¹⁰ Subsequently, another crystal structure of A₁R bound to a reversible antagonist, PSB36 (PDBID: 5N2S), was reported by Cooke and coworkers.¹¹ In these crystal structures, the A₁R was bound to an antagonist and was in the inactive state. Recently, the fully active structure of A₁R in complex with the endogenous agonist adenosine and heterotrimeric G_i protein (PDBID: 6D9H) was solved by Christopoulos and coworkers using Volta phase-plate cryo-electron microscopy (cryo-EM).¹² In this cryo-EM structure, the G_i protein engages the A₁R at the intracellular surface, and the intracellular side of the sixth transmembrane helix (TM6) of A₁R moves outward 10.5 Å to accommodate the G_i protein. These crystal structures provide an excellent molecular basis for computational studies and structure-based drug design of A₁R.

^a State Key Laboratory of Medicinal Chemical Biology, College of Pharmacy and Tianjin Key Laboratory of Molecular Drug Research, Nankai University, Haihe Education Park, 38 Tongyan Road, Tianjin 300353, People's Republic of China.
E-mail: jianpinglin@nankai.edu.cn, dongmeili@nankai.edu.cn

^b Pharmaceutical Intelligence Platform, Tianjin International Joint Academy of Biomedicine, Tianjin 300457, People's Republic of China

† Electronic supplementary information (ESI) available. See DOI: 10.1039/c9cp04060a

Over the past decades, the vast majority of the research on GPCR signaling was performed under the assumption that GPCRs exist and function as monomers. However, increasing evidence suggest that GPCRs can interact with one another to form homo-, heterodimers or even higher-order oligomers across the different classes of the GPCR superfamily.^{13–17} The A₁R has been proved experimentally with various biochemical and biophysical techniques to form homodimers, not only in cell cultures, but also in the brain cortex.^{18,19} Protomer–protomer interactions in A₁R dimers were shown to account for some of the pharmacological characteristics of agonist and antagonist binding, and thus the activation and signaling of A₁Rs.¹⁹ However, the cooperativity of the two protomers and its role in A₁R function and signal transduction are not yet fully understood.

MD simulations are an important tool to study the physical basis of the dynamic behavior and function of biomolecules.²⁰ There have been many MD studies in the past few years on GPCR in the monomeric unit, including our previous work on the glucagon receptor.^{21–28} However, there are far fewer MD studies on GPCR dimers than those on monomers.^{29–34} In addition, prior dimer simulations mainly focused on the dynamics and interactions with ligands of GPCRs,^{29,31,32} without consideration of the activation mechanism of GPCR dimers.^{30,33,34} In previous experimental studies, GPCRs were observed to activate on a millisecond timescale,³⁵ which is computationally expensive for conventional MD simulations. In addition, GPCR dimerization significantly increases the size of the simulation system, which is even more difficult for conventional MD to deal with. To improve the efficiency of conventional MD simulations, enhanced sampling techniques have been developed during the last several decades.^{36–38} With enhanced sampling techniques, researchers can simulate a biomolecule's long-timescale behavior on the basis of a relatively short simulation time. Among these techniques, a Gaussian accelerated MD (GaMD)^{39–41} was used to simulate GPCRs, providing important insight into GPCR signaling processes.⁴²

In the present study, we applied docking and metadynamics (metaMD) to identify the binding mode of 5'-N-ethylcarboxamidoadenosine (NECA), an analogue of adenosine, which is one of the most studied agonists of A₁R, in the orthosteric pocket of A₁R. Then, we applied MD and GaMD methods to simulate dimerization and its effect on the activation and conformational dynamics of A₁R. Our results suggest an asymmetrical activation mechanism of the homodimer and a negative cooperativity between the two protomers.

2. Materials and methods

2.1 System setup

The 3D structure of the A₁R monomer was extracted from the PDB bank crystal structure of the antagonist DU172-bound form (PDBID: 5UEN, chain A).¹⁰ T4 lysozyme in the crystal structure was removed and the missing intracellular loop 3 (ICL3) of the structure was built by homology modelling using the I-TASSER online program.⁴³ The protonation state for

titratable residues was determined using the H++ program⁴⁴ and the TLEAP module in AMBER18.⁴⁵

To investigate the activation process and the accompanying conformational change of A₁R, we docked NECA into the binding pocket formed by residues Thr91^{3,36}, Phe171^{ECL2}, Glu172^{ECL2}, Leu250^{6,51}, Asn254^{6,55}, Thr277^{7,42} and His278^{7,43} using AutoDock.⁴⁶ These residues are highly conserved in A₁R and A_{2A}R subtypes, and have been found to be crucial for NECA interaction.^{12,47,48} We chose the docking mode with the lowest free energy of binding from the top cluster given by AutoDock as the best docking mode, in which NECA had a similar conformation to that of the docking modes of adenosine to A₁R (PDBID: 6D9H) and NECA to A_{2A}R (PDBID: 2YDV).^{12,47}

We built a simulation system of NECA-bound A₁R monomer (NECA-A₁R-M) based on the docking structure. The structure was inserted into 100 Å × 100 Å 1-palmitoyl-2-oleylphosphatidylcholine (POPC) bilayers, and was solvated in TIP3P⁴⁹ water boxes with 0.15 M NaCl to neutralize the system. The NECA-A₁R-M system includes 111 932 atoms, and the dimensions of the whole system are 100 Å × 100 Å × 120 Å. A representative scheme of the NECA-A₁R-M system was shown in Fig. S1A (ESI†).

Further, three homodimer systems were set up, including A₁R homodimers in apo form (apo-A₁R), with a single NECA bound in one protomer (NECA-A₁R), and with two NECAAs bound in each protomer (dNECA-A₁R). The apo-A₁R structure was constructed using chain A and B in the DU172-bound crystal structure¹⁰ (PDBID: 5UEN) with DU172 removed. Then, we placed NECA into one protomer of apo-A₁R to obtain the NECA-A₁R structure (Fig. S1B, ESI†), and separately placed two NECAAs into both protomers of apo-A₁R to obtain the dNECA-A₁R structure (Fig. S1C, ESI†). The binding modes of the NECAAs in the NECA-A₁R and dNECA-A₁R protomers were the same as those determined from the docking results for the NECA-A₁R-M system. Then, each homodimer structure was inserted into 130 Å × 130 Å POPC bilayers, with water solvation (calculated using the TIP3P model) and 0.15 M NaCl. The structure of the NECA-A₁R system is shown in Fig. S2 (ESI†) as an example. The apo-A₁R, NECA-A₁R and dNECA-A₁R systems include 213 677, 213 715 and 213 753 atoms, respectively. The dimensions of each system are 130 Å × 130 Å × 130 Å.

2.2 Molecular dynamics simulations

The molecular dynamics simulations were carried out using the PMEMD module of AMBER18.⁴⁵ The AMBER FF14SB force field⁵⁰ was used for A₁R. We generated prmtop and inpcrd files for NECA using General AMBER Force Field⁵¹ (GAFF) with Antechamber of AMBER 18.⁴⁵ The AMBER lipid force field LIPID14⁵² was used for POPC. The time step was set to 2 fs for all simulations.

2.3 Conventional molecular dynamics

We first minimized each system for 10 000 steps. Then, thermalization of each system with heating from 0 to 310 K was carried out over 500 ps using the Langevin thermostat.⁵³ During thermalization, the protein, ligand and lipid head groups were fixed with a constraint of 50 kcal mol⁻¹ Å⁻². We then performed a series of equilibrations for each system. The POPCs were

equilibrated for 25 ns, and the A₁R and NECA were constrained with 50 kcal mol⁻¹ Å⁻². After that, the ICL3 and TM8 of A₁R were equilibrated for 50 ns, and the other residues of A₁R and NECA were constrained with 50 kcal mol⁻¹ Å⁻². Then, the whole system for each system was released and equilibrated for 20 ns with no constraints. Finally, 100 ns conventional MD simulations for NECA-A₁R-M, apo-A₁R, NECA-A₁R and dNECA-A₁R were performed at constant pressure (using an *NPT* ensemble). A 12 Å cut-off was set for the non-bonded interaction. The SHAKE⁵⁴ algorithm integration was used to constrain covalent bonds that involved hydrogen atoms and the Particle Mesh Ewald (PME)⁵⁵ algorithm was applied to treat long-range electrostatic interactions. The frames were saved every 5000 steps for analysis.

2.4 Metadynamics (metaMD)

To confirm the binding mode of NECA in A₁R, we also carried out well-tempered metadynamics⁵⁶ using the PLUMED 2.4a plugin⁵⁷ of AMBER18.⁴⁵ The last frame of the 20 ns conventional MD simulation of the NECA-A₁R-M system was used as the starting structure of the metaMD simulation. The parameter files for metaMD were created containing the collective variables (CVs) and the bias information. Specifically, CV₁ was the distance between the centers of mass (COMs) of NECA and the seven transmembrane helical bundles of A₁R along the direction perpendicular to the membrane (Z-direction). CV₁ was restrained at [-30 Å, 30 Å] to avoid NECA escaping into the cytoplasm. CV₂ was set as the distance between the COMs of NECA and the residues Thr91^{3,36}, Phe171^{ECL2}, Glu172^{ECL2}, Thr277^{7,42} and His278^{7,43} (Fig. S3, ESI†). In our docking mode, these five residues interact with NECA, and the distance between their COMs and NECA is very close. A Gaussian bias with a height of 1 kJ mol⁻¹ and width of 0.05 nm was deposited to activate the metaMD. The deposition interval was 1 ps and the bias factor was 15.

2.5 Gaussian accelerated molecular dynamics (GaMD)

To capture the more obvious effect of A₁R dimerization on activation, we carried out GaMD simulations⁵⁸ using the GaMD module in the graphics processing unit version of AMBER18.⁴⁵ Restarting from the last structure obtained from the 100 ns conventional MD simulations, we performed 10 ns conventional MD simulations for calculating the GaMD acceleration parameters and 50 ns equilibration after adding the boost potential. Then, we performed three independent 300 ns GaMD simulations for each of the apo-A₁R, NECA-A₁R and dNECA-A₁R systems. The frames were saved every 50 000 steps for analysis.

2.6 Trajectory analysis

The trajectories were analyzed with the VMD⁵⁹ and CPPTRAJ⁶⁰ tools in AMBER18.⁴⁵ Reweighting of the GaMD was performed with the PyReweighting⁶¹ toolkit. The atom distances and root-mean-square deviation (RMSD) were reweighted to compute the potential of mean force (PMF) profiles with a bin size of 0.35 Å.

2.7 Network analysis

To investigate the correlated motions among residues of A₁R, we performed network analysis.^{62,63} First, dynamic cross-correlation motions (DCCM) analysis was used to calculate the correlation matrixes between nodes centered by the C_α atoms of the A₁R residues in the MD trajectories with the Carma⁶⁴ program in the NetworkView plugin of VMD.⁵⁹ Then, the edges were used to connect the nodes, which have a distance of less than 4.5 Å for more than 75% of the simulation time. The edges were calculated on the basis of the correlation matrix, and the network map was formed by the connection of edges. Finally, we divided the network map into different communities using the Girvan–Newman algorithm;⁶⁵ the nodes in a community were highly connected and the nodes in different communities were loosely connected. The community network analysis was carried out with the Gncommunities program in the NetworkView plugin of VMD.⁵⁹

3. Results and discussion

3.1 Binding mode of NECA in A₁R

Agonists of adenosine receptors can influence intracellular signaling by changing the conformational states and stabilizing the active state of the receptor. To investigate the dynamics of the different conformational states and reach the active state of A₁R, we studied the conformational dynamics of A₁R in the apo and agonist-bound forms.

Based on the structure of the antagonist DU172-bound A₁R homodimer, which is considered in the inactive state, we built three homodimer systems: apo-A₁R, NECA-A₁R (with NECA binding in one protomer of the A₁R homodimer) and dNECA-A₁R (with NECA binding in each protomer of the A₁R homodimer). Then, we performed three parallel 100 ns conventional MD simulations for each system. The RMSD of the protein of each protomer was calculated for each system based on the initial X-ray crystallographic structure (Fig. S4A–C, ESI†); the averaged values of the three parallel trajectories are listed in Table S1 (ESI†). The results show that each system achieved equilibrium during the conventional MD simulation. The RMSD of NECA (relative to the docking pose coordinates) inside the orthosteric binding site was measured during the conventional MD simulation of NECA-A₁R and dNECA-A₁R systems (Fig. S4D–F (ESI†) show representative trajectories of each system and Table S1 (ESI†) contains the averaged values of the three parallel trajectories). After the 20 ns equilibration and 100 ns conventional MD simulation, NECA achieved a stable binding mode against A₁R. The last snapshot of conventional MD simulation was extracted from the trajectory of NECA-A₁R for the binding-mode analysis.

The binding mode of NECA in A₁R is shown in Fig. 1A, and the 2D structure and atom names for NECA are shown in Fig. S5 (ESI†). NECA occupies the orthosteric binding pocket of A₁R, with the purine group π-stacking with Phe171^{ECL2} (the distance between the centers of the phenyl group of Phe171^{ECL2} and the purine group of NECA is 3.8 Å). Adjacent to Phe171^{ECL2}, the carbonyl oxygen of Glu172^{ECL2} forms a salt bridge with the N⁶ of NECA with a distance of 3.0 Å. Asn254^{6,55} locates the purine

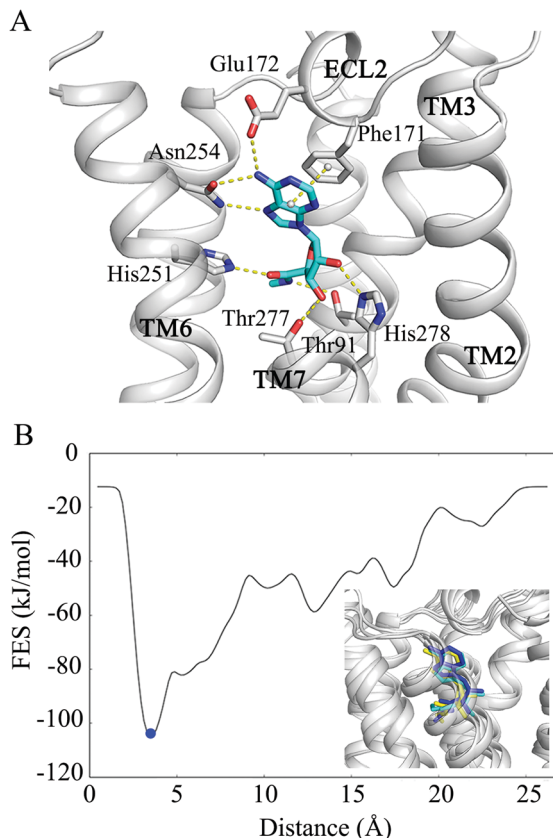


Fig. 1 (A) Binding mode of NECA in A₁R. Hydrogen bonds between NECA and A₁R are represented by dashed lines. The centers of the phenyl group of Phe171^{ECL2} and the purine group of NECA are shown with white dots, and the π-tacking is also represented by dashed lines. (B) Free energy surface associated with NECA–A₁R interactions as a function of the distance between the COMs of NECA and the pocket composed of residues Thr91^{3.36}, Phe171^{ECL2}, Glu172^{ECL2}, Thr277^{7.42} and His278^{7.43}. Comparison of the structures of our binding site, the last snapshot of cMD simulation and minimum A is shown in the lower right corner. The A₁R structure is shown in cartoon and colored in silver, the NECA in our binding site, in the last snapshot of cMD simulation and minimum A are shown in stick and colored in cyan, yellow and blue, respectively.

ring of NECA through two hydrogen bonds of 2.9 Å (between the acylamino δ1-oxygen of Asn254^{6.55} and the N⁶ of NECA) and 3.0 Å (between the acylamino δ2-nitrogen of Asn254^{6.55} and the N⁷ of NECA). The ribose moiety of NECA is accommodated by two hydrogen bonds with the side chains of Thr277^{7.42} (the distance between the hydroxyl oxygen of Thr277^{7.42} and the O^{3'} of NECA is 2.8 Å) and His278^{7.43} (the distance between the imidazole ε-nitrogen of His278^{7.43} and O^{2'} of NECA is 2.7 Å). Additionally, the carboxamide group of NECA points into the A₁R pocket, and forms two hydrogen bonds with Thr91^{3.36} (the distance between the hydroxyl oxygen of the Thr91^{3.36} side chain and the N^{5'} of NECA is 3.3 Å) and His251^{6.52} (the distance between the imidazole ε-nitrogen of His251^{6.52} and the O^{5'} of NECA is 2.7 Å). Thr91^{3.36} and Thr277^{7.42} have been shown to have pivotal roles in the binding of NECA with A₁R.⁶⁶ The residues involved in our binding mode are consistent with previous research on pockets of agonists in both A₁R and A_{2A}R.^{12,47}

We calculated the distances for these protein–ligand interactions through the GaMD simulations. Table S2 (ESI†) shows the averaged values of the three parallel trajectories. It can be seen that the interactions between NECA and the related residues exist through all GaMD simulations.

To confirm the binding mode obtained by the docking study, we performed 100 ns conventional MD simulations for the NECA–A₁R–M system. From the time dependence of the RMSD of NECA relative to the docking pose shown in Fig. S6 (ESI†), we can conclude that our binding mode was stable. Then, we performed metaMD simulations for the NECA–A₁R–M system. Fig. 1B depicts the free-energy surface of the NECA–A₁R interactions as a function of the distance between the COMs of NECA and the binding pocket composed of residues Thr91^{3.36}, Phe171^{ECL2}, Glu172^{ECL2}, Thr277^{7.42} and His278^{7.43}. The minimum of the free-energy surface reveals that NECA binds to A₁R with a distance of about 3 Å between the COMs of NECA and the pocket composed of Thr91^{3.36}, Phe171^{ECL2}, Glu172^{ECL2}, Thr277^{7.42} and His278^{7.43}. The structure of the minimum in the free-energy surface of metaMD simulation aligns well with the binding pose from the docking study and the 100 ns conventional MD simulation with RMSDs of 0.9 and 1.6 Å (compared with the last snapshot) for nonhydrogen atoms of NECA (see the aligned structures in the lower-right corner of Fig. 1B).

3.2 Activation of the A₁R homodimer

To study the dimerization effects on the process of activation of A₁R, we performed 300 ns GaMD simulations to enhance conformational space sampling on each system after the conventional MD simulations. To ensure the reproducibility of the results, three parallel MD simulations were performed for each of the apo-A₁R, NECA–A₁R and dNECA–A₁R systems. The results between the three parallel simulations were similar. Thus, we presented the results of one representative trajectory and listed the averaged values of the three parallel trajectories in Table 1.

Several activation features for class A GPCRs were revealed by previous experimental research.⁶⁷ A key characteristic of the A₁R activation is a large outward movement of the cytoplasmic end of TM6 by 10.5 Å to accommodate the C-terminal helix of G_i (known as the α5 helix of the G_i protein), which results in activation of the G protein.¹² Additional fundamental features of receptor activation previously observed are rearrangements of the DRY and KxxK motifs that are conserved in class A GPCRs.^{68–70} Moreover, the salt bridge (ionic lock) formed by Arg105^{3.50} or Arg108^{3.53} (Arg105^{3.50}/Arg108^{3.53}) and Glu229^{6.30} observed in the active A₁R is broken, and R105^{3.50} of the DRY motif extends towards TM7 to form a lid over the G_i α5-helix.^{10,11} Therefore, we monitored the distance between the cytoplasmic ends of TM3 and TM6 by measuring the distance between the C_α atoms of Ile111^{3.56} and Gln223^{6.24} (*i.e.*, the TM3–TM6 distance) and the RMSD of the DRY motif (DRY RMSD) relative to the initial crystal structure for the two protomers (P₁ and P₂) in each system. Then, we calculated the PMFs for the TM3–TM6 distance and the RMSD for the DRY motif for the apo-A₁R system, NECA–A₁R system, and dNECA–A₁R system. We also measured the RMSD of the KxxK motif (KxxK RMSD) relative to the initial

Table 1 Averaged values and standard deviations of the TM3-TM6 distance, the RMSD of the DRY motif relative to the inactive starting structure, the N–O distance between the guanidinium of Arg105^{3.50}/Arg108^{3.53} and the carboxyl of Glu229^{6.30}, the RMSD of the KxxK motif relative to the inactive starting structure for each protomer over the three parallel GaMD trajectories

System	TM3-TM6 (Å)		DRY RMSD (Å)		Arg105 ^{3.50} /Arg108 ^{3.53} -E229 ^{6.30} (Å)		RxxR RMSD (Å)	
	Average	SD	Average	SD	Average	SD	Average	SD
P ₁ of apo-A ₁ R	16.2	0.2	1.4	0.2	2.8	0.1	2.8	0.2
P ₂ of apo-A ₁ R	18.0	0.5	0.9	0.1	2.9	0.02	2.2	0.1
P ₁ of NECA-A ₁ R	18.4	2.2	1.1	0.1	3.0	0.2	2.9	0.4
P ₂ of NECA-A ₁ R ^a	24.4	0.9	1.8	0.1	8.8	0.6	5.3	1.2
P ₁ of dNECA-A ₁ R ^b	21.6	2.2	2.9	0.5	8.7	1.1	7.5	0.8
P ₂ of dNECA-A ₁ R	16.2	1.7	1.2	0.1	3.1	0.5	2.3	0.1

^a The snapshots of the three parallel GaMD simulations in 260–290 ns, 110–140 ns, and 200–230 ns which correspond to the active state for the NECA-A₁R system are extracted from the trajectories to calculate the distances, RMSD and angle here. ^b The snapshots of the three parallel GaMD simulations in 235–265 ns, 130–160 ns and 230–260 ns which correspond to the active state for the dNECA-A₁R system are extracted from the trajectories to calculate the distances, RMSD and angle here.

Published on 03 October 2019. Downloaded on 1/2/2020 7:21:44 PM.

crystal structure, and monitored the ionic lock measured by the N···O distance between the guanidinium of Arg105^{3.50}/Arg108^{3.53} and the carbonyl of Glu229^{6.30} during conventional MD and GaMD simulations. We captured the activation process, which was accompanied by similar characteristics for both the NECA-A₁R and dNECA-A₁R systems in the 300 ns GaMD simulations.

Asymmetrical activation of the NECA-A₁R system. The features of the active state for the A₁R homodimer bound with a single NECA are depicted in Fig. 2. In the NECA-A₁R system, the PMF map clearly reveals different conformational states for P₁ and P₂ (Fig. 2A and B). For P₁, the TM3-TM6 distance is about 16.1 Å (Fig. 2E), which is similar to the TM3-TM6 distance of 17.2 Å in the inactive crystal structure. The DRY RMSD of P₁ is 1.1 Å (Fig. 2F). The Arg105^{3.50}/Arg108^{3.53}-Glu229^{6.30} ionic lock

is closed (with a distance of 2.9 Å in Fig. 2G). The KxxK RMSD is 3.0 Å (Fig. 2H). For P₂, the TM3-TM6 distance increases to 23.4 Å during the 260–290 ns of the GaMD simulation (Fig. 2E). The DRY RMSD increases to 1.9 Å (Fig. 2F). This means that the snapshots in the 260–290 ns of P₂ are in the active state of A₁R. Correspondingly, the Arg105^{3.50}/Arg108^{3.53}-Glu229^{6.30} ionic lock breaks (with a distance of 9.3 Å in Fig. 2G), and the KxxK motif adopt a fully extended conformation with a RMSD of 6.7 Å (Fig. 2H). We clustered the snapshots within the GaMD simulation into three clusters based on the TM3-TM6 distance of P₂ for NECA-A₁R (P₁ for dNECA-A₁R). The central structure of the cluster with the largest TM3-TM6 distance was chosen as the representative structure for the NECA-A₁R system (dNECA-A₁R system). The representative structures and features of the inactive P₁, and the active state of P₂ relative to the initial

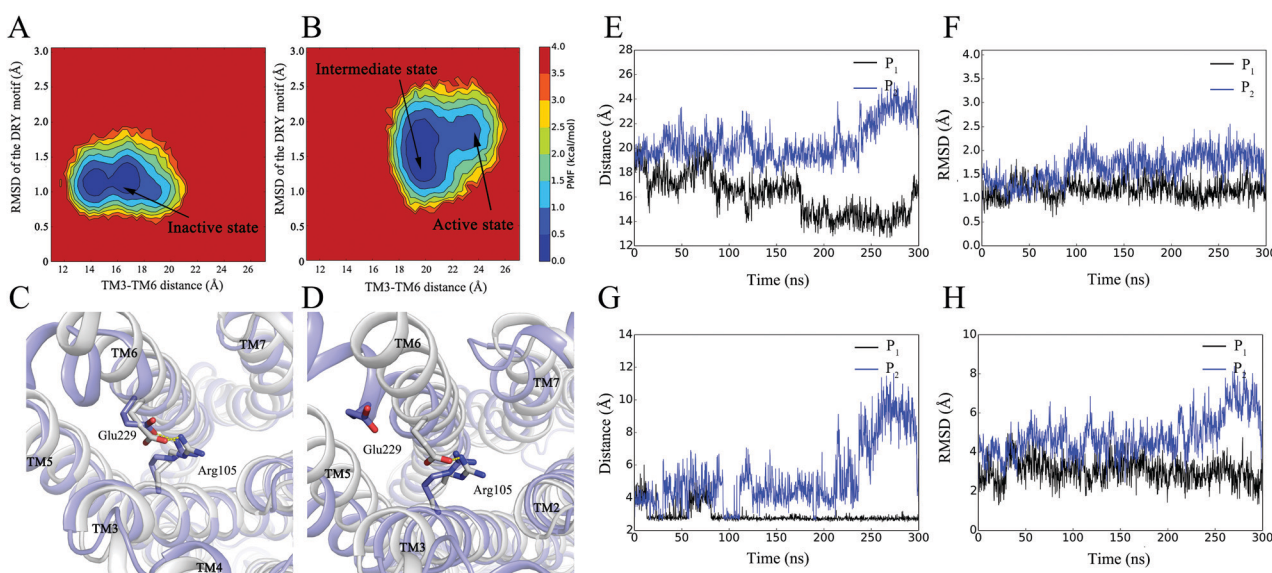


Fig. 2 Potential of mean force (PMF) calculated for the TM3-TM6 distance vs. the RMSD of the DRY motif relative to the inactive starting structure for (A) P₁ and (B) P₂ of the NECA-A₁R system. Representative structures of the cytoplasmic side of (C) P₁ and (D) P₂ of the NECA-A₁R system (colored in blue) aligned to the inactive crystal structure (color in silver). A₁R is displayed in cartoon, residues Arg105^{3.50} and Glu229^{6.30} are displayed in ball-and-stick. Time dependences of (E) TM3-TM6 distance, (F) RMSD of the DRY motif relative to the inactive starting structure, (G) the N–O distance between the guanidinium of Arg105^{3.50}/Arg108^{3.53} and the carboxyl of Glu229^{6.30}, and (H) RMSD of the KxxK motif relative to the inactive starting structure in the GaMD simulation of the NECA-A₁R system.

inactive crystal structure are demonstrated in Fig. 2C and D, respectively. During the rest time of the simulation, P₂ was in an intermediate state with a TM3–TM6 distance of 20.2 Å and a DRY RMSD of 1.6 Å.

To investigate the roles of water molecules during the activation of the A₁R homodimer, we monitored the average of number of water molecules in the G-protein binding crevice, which was composed of the intracellular side of the transmembrane helices. During the 260–290 ns, 110–140 ns, and 200–230 ns GaMD simulations of NECA–A₁R, which corresponds to P₂ in its active state, there are 20 water molecules in the G-protein binding crevice of P₂; by contrast, there are 15 water molecules in P₁ during the 300 ns GaMD simulations. For dNECA–A₁R, there are 22 and 18 water molecules in the G-protein binding crevice for P₁ and P₂, respectively (Table S3, ESI†). This means that more water molecules enter the G-protein binding crevice in P₂ of NECA–A₁R and P₁ of dNECA–A₁R with the outward tilt of the intracellular end of TM6.

To summarize, in the GaMD simulation of the NECA–A₁R system, P₁ (bound with NECA) preserves its initial inactive conformational state, whereas P₂ (with no ligand) achieves an active state during the 260–290 ns of the GaMD simulation. This suggests an asymmetrical activation mechanism, which is consistent with the GPCR dimer activation observed in previous experimental studies.^{15,71,72} The results of the other two parallel GaMD simulations of the NECA–A₁R system are shown in Fig. S7 and S8 (ESI†).

Asymmetrical activation of the dNECA–A₁R system. In the 300 ns GaMD simulation of the dNECA–A₁R system, we captured the activation process. Fig. 3 depicts the features of the activation process and the representative structures of each state. The PMF

maps in Fig. 3A and B clearly show different conformational states of P₁ and P₂ of the dNECA–A₁R system. P₁ achieves an active state during the 235–265 ns of the GaMD simulation. In the active state of P₁, the TM3–TM6 distance increases to 21.1 Å (Fig. 3E), the DRY RMSD increases to 2.9 Å (Fig. 3F), the Arg105^{3.50}/Arg108^{3.53}–Glu229^{6.30} ionic lock breaks (with a distance of 9.9 Å in Fig. 3G), and the KxxK RMSD increases to 7.17 Å (Fig. 3H). In the rest time of simulation, the P₁ was in an intermediate state, with a TM3–TM6 distance of 18.3 Å and a DRY RMSD of 2.5 Å. P₂ stays in the inactive state throughout the 300 ns GaMD simulation, with a TM3–TM6 distance of 17.9 Å (Fig. 3E) and a DRY RMSD of 1.5 Å (Fig. 3F). The Arg105^{3.50}/Arg108^{3.53}–Glu229^{6.30} ionic lock is still closed (with a distance of 3.6 Å in Fig. 3G), and the KxxK RMSD is 2.42 Å (Fig. 3H).

To summarize, in the activation of the dNECA–A₁R system, P₁ achieves an active state in 235–265 ns, and P₂ stays in the inactive state. The activation of one of the two identical protomers in the A₁R homodimer is consistent with the asymmetrical activation observed in experimental studies,¹⁵ and indicates a negative cooperativity between P₁ and P₂ in the activation process of dNECA–A₁R. Previous experimental research has provided evidence for negative cooperativity of GPCR dimers.^{73–75} The results of the other two parallel GaMD simulations of the dNECA–A₁R system are shown in Fig. S9 and S10 (ESI†).

In the apo-A₁R system (Fig. S11, ESI†), the TM3–TM6 distances are 16.1 and 17.9 Å for P₁ and P₂, and the DRY RMSDs are 1.2 and 1.0 Å for P₁ and P₂ during the GaMD simulation. The Arg105^{3.50}/Arg108^{3.53}–Glu229^{6.30} ionic locks are closed (2.9 and 2.9 Å for P₁ and P₂), and the KxxK RMSD is 2.63 and 2.19 Å for P₁ and P₂. These results indicate that the apo-A₁R system stays in the inactive state during the GaMD simulation.

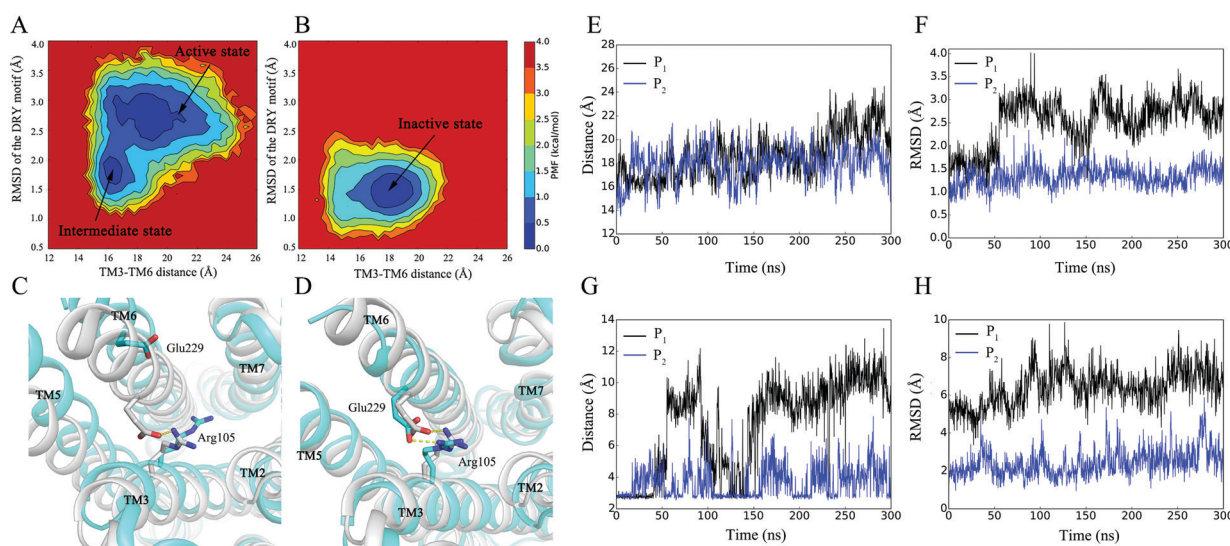


Fig. 3 Potential of mean force (PMF) calculated for the TM3–TM6 distance vs. the RMSD of the DRY motif relative to the inactive starting structure for (A) P₁ and (B) P₂ of the dNECA–A₁R system. Representative structures of the cytoplasmic side of (C) P₁ and (D) P₂ of the dNECA–A₁R system (colored in blue) aligned to the inactive crystal structure (color in silver). A₁R is displayed in cartoon, and residues Arg105^{3.50} and Glu229^{6.30} are displayed in ball-and-stick. Time dependences of (E) TM3–TM6 distance, (F) RMSD of the DRY motif relative to the inactive starting structure, (G) the N–O distance between the guanidinium of Arg105^{3.50}/Arg108^{3.53} and the carboxyl of Glu229^{6.30} and (H) RMSD of the KxxK motif relative to the inactive starting structure in the GaMD simulation of the dNECA–A₁R system.

3.3 Cross-correlated motions

To analyze the dynamic correlation between the residues of the A₁R homodimer, we carried out DCCM analysis for the apo-A₁R, NECA-A₁R and dNECA-A₁R systems. In the NECA-A₁R system, the DCCM analysis was based on the 30 ns GaMD trajectories in its active state (from 260 to 290 ns); in the dNECA-A₁R system, the 30 ns GaMD trajectories in its active state (from 235 to 265 ns) were chosen. For comparison, the analysis for the apo-A₁R system was based on the last 30 ns GaMD trajectories. Fig. 4 depicts the DCCM maps of the NECA-A₁R and dNECA-A₁R systems. The highly correlated residues in the DCCM analysis are listed in Table S4 (ESI†).

In the NECA-A₁R system, the correlation coefficients of residues 42–54 in TM2 (*i.e.* Asp42^{2,37} to Ala54^{2,49}) and residues 200–238 in TM5/TM6 (*i.e.* Tyr200^{5,58} to Leu238^{6,39}) are higher in P₁ than those in P₂, and the correlation coefficient of residues 98–110 in TM3 (*i.e.* Leu96^{3,43} to Lys110^{3,55}) and residues 226–242 in TM6 (*i.e.* Tyr226^{6,27} to Leu242^{6,43}) are also higher in P₁ than those in P₂ (see the small boxes in Fig. 4A). These results indicate that the coupling of TM2 and TM5/TM6 and the coupling of TM3 and TM6 in the intracellular side are stronger in P₁ than in P₂. The weaker intracellular coupling between TM2/TM3 and TM5/TM6 in P₂ is caused by the outward movement of the TM6 intracellular side (which is a specific characteristic of activation).

In the dNECA-A₁R system, the correlation coefficients of residues 44–55 in TM2 and residues 200–240 in TM5/TM6, and the correlation coefficients of residues 95–110 in TM3 and residues 226–244 in TM6 are lower in P₁ than in P₂ (see the little boxes in Fig. 4B), meaning that the couplings between the intracellular side of TM2/TM3 and TM5/TM6 are weaker in P₁ than in P₂. The activation of P₁ (with TM6 moving outward) weakens the intracellular coupling between TM2/TM3 and TM5/TM6 in P₁.

In the apo-A₁R system, both protomers show strong couplings between TM2/TM3 and TM5/TM6, similar to those of the inactive P₁ in the NECA-A₁R system and the inactive P₂ in

the dNECA-A₁R system (Fig. S12, ESI†). The results of the other two parallel GaMD simulations of the NECA-A₁R and dNECA-A₁R systems are shown in Fig. S13 (ESI†).

3.4 Dynamic network

To gain insight into the conformational changes during the activation process of A₁R homodimers, we performed community network analysis based on the trajectories of DCCM analysis for the NECA-A₁R and dNECA-A₁R systems. Residues are divided into different communities according to their connections. Edges were used to connect pairs of residues; the weight of the edge reflects the strength of the residue connections. The edges with a weight of less than 0.5 were considered to be strong connections. Fig. 5 shows the communities and the connections in the intracellular sides of the NECA-A₁R and dNECA-A₁R systems.

In the NECA-A₁R system, the intracellular sides of the TMs in P₁ are clustered around two different communities (Fig. 5A): Community 1 (composed of TM1 and TM7) and Community 2 (composed of TM2, TM3, TM4, TM5 and TM6). TM3 and TM5 connect strongly *via* the contacts between residues Leu99^{3,44}, Ala102^{3,47}, Arg105^{3,50}, Tyr106^{3,51}, Val109^{3,54} and Lys110^{3,55} in TM3, and residues Leu195^{5,53}, Met196^{5,54}, Ile199^{5,57}, Tyr200^{5,58}, Glu202^{5,60}, Val203^{5,61}, Leu206^{5,64}, Ile207^{5,65} and Gln210^{5,68} in TM5. TM3 and TM6 connect *via* the contacts between residues Leu98^{3,43}, Arg105^{3,50} and Arg108^{3,53} in TM3, and residues Glu229^{6,30}, Ile232^{6,33} and Leu236^{6,37} in TM6. These intensive connections in the intracellular side of TM3 and TM5/TM6 preserve P₁ in the inactive state. By contrast, the intracellular sides of TMs in P₂ are clustered around three different communities (Fig. 5B): Community 1 (composed of TM1 and TM7), Community 2 (composed of TM2, TM3 and TM4) and Community 3 (composed of TM5 and TM6). The intracellular sides of TM5 and TM6 separate from the community composed of TM2, TM3 and TM4, and become a single community. Most of the connections between TM3 (in Community 2 of P₂) and TM5/TM6 (in Community 3 of P₂) in P₁ are lost in the residues of P₂. In P₂, TM3 (in Community 2) and TM5

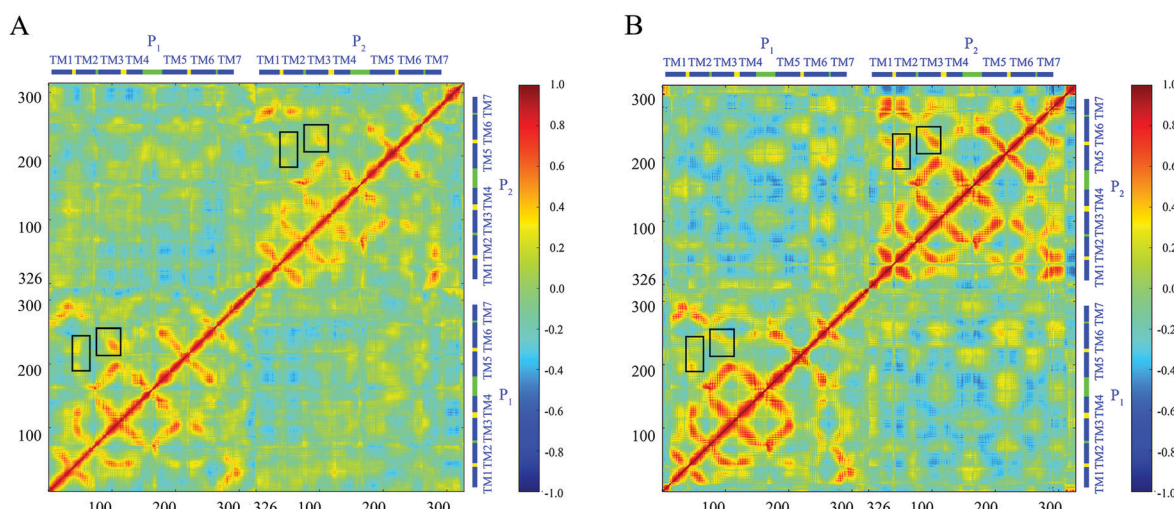


Fig. 4 Dynamic cross-correlations map for (A) the NECA-A₁R system and (B) the dNECA-A₁R system. The color scale is shown on the right changing from red to (highly positive correlations) to blue (highly negative correlations).

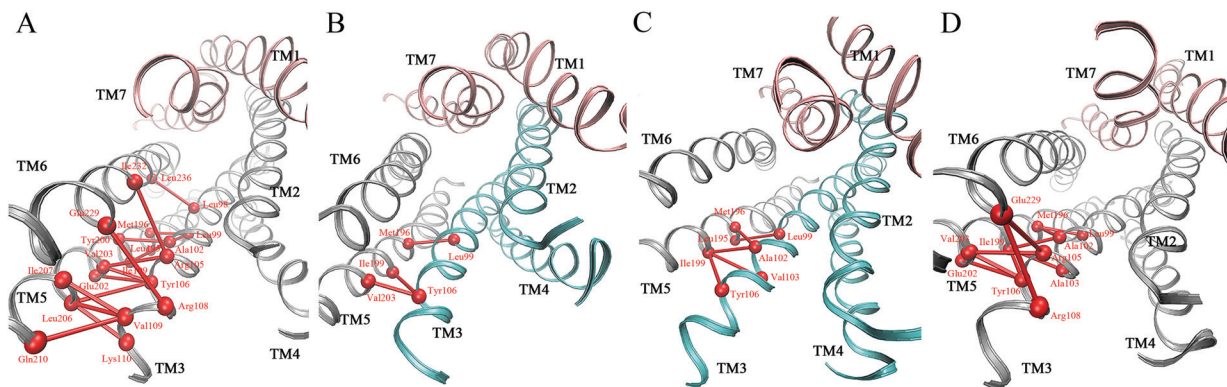


Fig. 5 The networks for the intracellular side of (A) P₁ and (B) P₂ of the NECA–A₁R system and (C) P₁ and (D) P₂ of the dNECA–A₁R system.

(in Community 3) connect loosely *via* the Leu99^{3.44}–Met196^{5.54}, Tyr106^{3.51}–Val203^{5.61} and Tyr106^{3.51}–Ile199^{5.57} contacts. This is in accordance with the outward movement of the TM6 intracellular side for the activation of P₂.

In the dNECA–A₁R system, the cluster of communities for intracellular sides of TMs of P₁ (Fig. 5C) is similar to that of P₂ in the NECA–A₁R system. Community 2 and Community 3 are connected *via* the Leu99^{3.44}–Leu195^{5.53}, Ala102^{3.47}–Met196^{5.54}, Ala102^{3.47}–Ile199^{5.57}, Val103^{3.48}–Ile199^{5.57} and Tyr106^{3.51}–Ile199^{5.57} interactions. The loose connections among the intracellular sides of TMs contribute to the activation of P₁. In P₂ (Fig. 5D), the cluster of communities is similar to that of P₁ in the NECA–A₁R system. Strong connections are observed between the intracellular sides of TM3 and TM5/TM6 *via* residues Leu99^{3.44}, Ala102^{3.47}, Val103^{3.48}, Arg105^{3.50}, Tyr106^{3.51} and Arg108^{3.53} in TM3, residues Leu195^{5.53}, Met196^{5.53}, Tyr200^{5.58}, Glu202^{5.60} and

Val203^{5.61} in TM5 and residue Glu229^{6.30} in TM6. These strong connections result in P₂ remaining in the inactive state.

To summarize, the connections between the intracellular sides of the TMs of P₁ and P₂ are different in the asymmetrical activation of the A₁R homodimer. In contrast to the strong connections in P₁ of NECA–A₁R and P₂ of dNECA–A₁R, the connections in P₂ of NECA–A₁R and P₁ of dNECA–A₁R are weak, owing to the outward movement of the TM6 intracellular side and activation of the corresponding protomer. The results of the other two parallel GaMD simulations of the NECA–A₁R and dNECA–A₁R systems are listed in Tables S5 and S6 (ESI[†]).

3.5 TM rearrangements in the activation of the A₁R homodimer

The distances between the COMs of P₁ and P₂ (P₁–P₂ distance) in the NECA–A₁R, dNECA–A₁R and apo-A₁R systems were

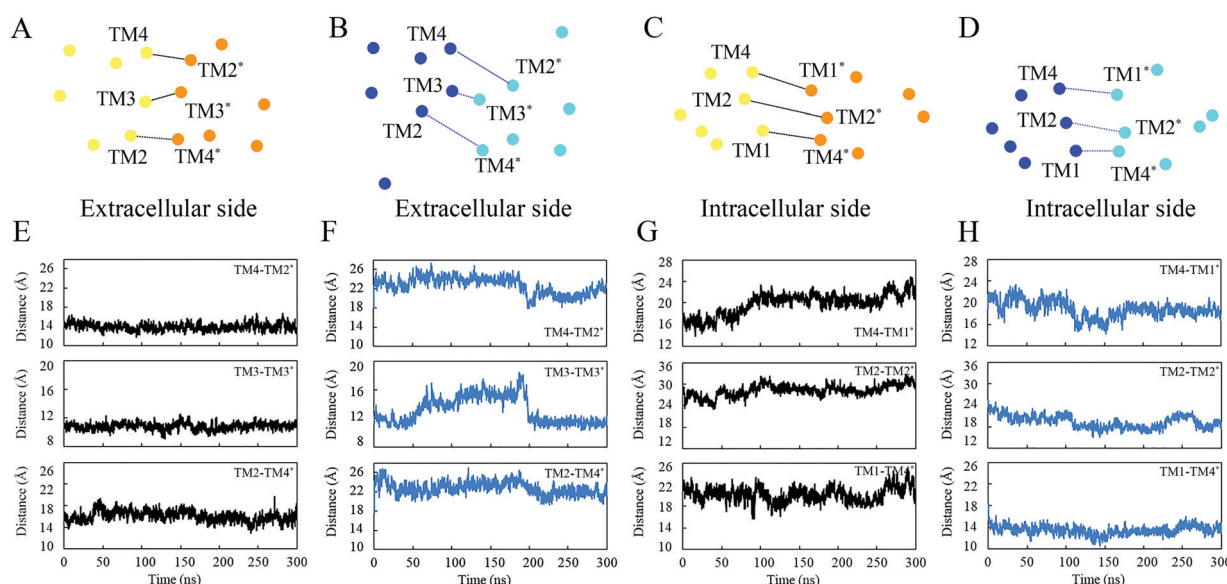


Fig. 6 Projections in the xy-plane of the (A) extracellular end of TMs of NECA–A₁R, (B) extracellular end of TMs of dNECA–A₁R, (C) intracellular end of TMs of NECA–A₁R and (D) intracellular end of TMs of dNECA–A₁R system. Time dependences of the (E) TM2–TM4* distance, TM3–TM3* distance and TM4–TM2* distance in the extracellular side of NECA–A₁R, (F) TM2–TM4* distance, TM3–TM3* distance and TM4–TM2* distance in the extracellular side of dNECA–A₁R, (G) TM1–TM4* distance, TM2–TM2* distance and TM4–TM1* distance in the intracellular side of NECA–A₁R and (H) TM1–TM4* distance, TM2–TM2* distance and TM4–TM1* distance in the intracellular side of dNECA–A₁R.

monitored during the GaMD simulations. The averaged P₁-P₂ distance in the apo-A₁R system is 33.1 Å, which is very close to the distances between the protomers in the β₁- and β₂-adrenergic receptor homodimers.⁷⁶ In the NECA-A₁R and dNECA-A₁R systems, the averaged P₁-P₂ distances are 35.6 and 35.2 Å, which is larger than that of apo-A₁R system (the averaged distances over the three parallel GaMD trajectories are shown in Table S7, ESI[†]). Thus, large conformational rearrangements of TMs occur in the activation process of the NECA-A₁R and dNECA-A₁R systems.

To investigate the mechanism of the asymmetrical activation observed in the NECA-A₁R and dNECA-A₁R systems, we monitored the distances between the TMs (TM2, TM3, TM4 of P₁ and TM2*, TM3*, TM4* of P₂ in the extracellular side and TM1, TM2, TM4 of P₁ and TM1*, TM2*, TM4* of P₂ in the intracellular side) in the interface of the A₁R homodimer. Fig. 6 shows the projections of the NECA-A₁R and dNECA-A₁R systems in both the extracellular and intracellular sides. The results for three parallel trajectories of each system are similar, and the averaged distances are shown in Table 2.

Extracellular side. In the extracellular side, the TM2-TM4*, TM3-TM3* and TM4-TM2* distances are shorter in the NECA-A₁R system (Fig. 6A and E, with averaged values of 16.1, 10.8 and 14.0 Å) than those in the dNECA-A₁R system (Fig. 6B and F, with averaged values of 22.7, 13.2 and 22.7 Å). This indicates closer and stronger connections of the extracellular side between protomers of the NECA-A₁R system than between those of the dNECA-A₁R system. The difference may be due to the NECA binding to the extracellular part of the TMs in one (the NECA-A₁R system) or both protomers (the dNECA-A₁R system). Binding with NECA in P₁ in the NECA-A₁R system breaks of the symmetry of the A₁R homodimer. In the NECA-A₁R system, NECA binds to P₁ and induces the activation of P₂ through the strong connections between the two protomers. The closer connection of the extracellular side strongly influences the asymmetric activation process for the homodimer.

Intracellular side. In the intracellular side, the TM1-TM4*, TM2-TM2* and TM4-TM1* distances are shorter in the dNECA-A₁R system (Fig. 6C and G, with averaged values of 13.5, 19.4 and 18.8 Å) than those in the NECA-A₁R system (Fig. 6D and H, with averaged values of 19.9, 28.3 and 20.2 Å). The shorter distances of the dNECA-A₁R system reflect the strong connections and influence of the two protomers. In the activation process of the dNECA-A₁R system, the conformational

Table 2 Averaged values of the TM2-TM4* distance, TM3-TM3* distance and TM4-TM2* distance in the extracellular side, and TM1-TM4* distance, TM2-TM2* distance and TM4-TM1* distance in the intracellular side of NECA-A₁R and dNECA-A₁R over the three parallel GaMD trajectories

Distance	NECA-A ₁ R (Å)		dNECA-A ₁ R (Å)	
	Average	SD	Average	SD
TM2-TM4* _{extra}	14.0	0.3	22.3	0.3
TM3-TM3* _{extra}	11.0	0.7	11.3	1.8
TM4-TM2* _{extra}	16.8	2.0	21.9	0.8
TM1-TM4* _{intra}	21.0	0.7	20.1	2.0
TM2-TM2* _{intra}	26.5	1.5	22.1	2.3
TM4-TM1* _{intra}	17.7	1.9	14.1	0.6

changes of P₁ in the intracellular ends influence the TM rearrangements of P₂ owing to the short distances and strong connections in the interface of the homodimer. The shorter distances and stronger connections at the intracellular side are the intrinsic reason for the negative cooperativity between P₁ and P₂ in the activation process of the dNECA-A₁R system.

4. Conclusions

In this work, we studied the binding mode of the agonist NECA to A₁R and explored the activation mechanism of the homodimer of A₁R. Conventional MD and GaMD methods were used to illustrate the activation mechanism and conformational changes in the activation process of the A₁R homodimer.

In the orthosteric pocket, NECA binds to A₁R mainly through π-stacking with Phe171^{ECL2} and hydrogen bonding with Thr91^{3,36}, Glu172^{ECL2}, His251^{6,52}, Asn254^{6,55}, Thr277^{7,42} and His278^{7,43}. This binding mode is similar to that of adenosine binding to A₁R and NECA binding to A_{2A}R in previously reported crystal structures. The A₁R homodimer can be activated by one or two NECA agonists occupied in its orthosteric pocket in one or both protomers. In the NECA-A₁R system, NECA binds to one protomer of the A₁R homodimer and induces the activation of the other protomer. This suggests an asymmetrical activation mechanism of the A₁R homodimer. In the dNECA-A₁R system, with two NECAs bound to each protomer, only one protomer is activated. This is consistent with the asymmetrical activation mechanism and indicates a negative cooperativity between the two protomers. The activation of the protomer is characterized by the outward movement of the extracellular end of TM6, the breaking of the Arg105^{3,50}/Arg108^{3,53}-Glu229^{6,30} salt bridge (ionic lock) and the rearrangements of the DRY and KxxK motifs. Owing to the outward movement of the TM6 intracellular end, the dynamic cross-correlations and the connections among the TMs of the activated protomer in the extracellular side become weaker than those in the inactive protomer. Large conformational rearrangements of TMs at the homodimer interface, which are characteristic of the shorter distances and stronger connections between TMs at the extracellular side of NECA-A₁R and intracellular side of dNECA-A₁R, occur in the activation process of A₁R homodimers in our GaMD simulation, and help facilitate the asymmetric activation process.

The results in the present study provide insight into the effect of dimerization on the activation of A₁R. Knowledge of the activation mechanism in dimers, and the dimerization effect for the signal transduction for A₁R would facilitate the future development of drug candidates for A₁R dimers.

Conflicts of interest

There are no conflicts to declare.

Acknowledgements

This study was supported by the National Key R&D Program of China (No. 2017YFC1104401).

Notes and references

- Published on 03 October 2019. Downloaded on 1/2/2020 7:21:44 PM.
- 1 S. Moro, G. Spalluto and K. A. Jacobson, *Trends Pharmacol. Sci.*, 2005, **26**, 44–51.
 - 2 R. Romagnoli, P. G. Baraldi, A. R. Moorman, P. A. Borea and K. Varani, *Future Med. Chem.*, 2015, **7**, 1247–1259.
 - 3 S. Kashfi, K. Ghaedi, H. Baharvand, M. H. Nasr-Esfahani and M. Javan, *Mol. Neurobiol.*, 2017, **54**, 8128–8139.
 - 4 J. Chen, H. K. Eltzschig and B. B. Fredholm, *Nat. Rev. Drug Discovery*, 2013, **12**, 265–286.
 - 5 K. A. Jacobson and Z. Gao, *Nat. Rev. Drug Discovery*, 2006, **5**, 247–264.
 - 6 M. Mansourian, K. Mahnam, A. Madadkar Sobhani, A. Fassihi and L. Saghaie, *Med. Chem. Res.*, 2015, **24**, 3645–3659.
 - 7 A. T. N. Nguyen, J.-A. Baltos, T. Thomas, T. D. Nguyen, L. L. Muñoz, K. J. Gregory, P. J. White, P. M. Sexton, A. Christopoulos and L. T. May, *Mol. Pharmacol.*, 2016, **90**, 703–714.
 - 8 A. T. N. Nguyen, E. A. Vecchio, T. Thomas, T. D. Nguyen, L. Aurelio, P. J. Scammells, P. J. White, P. M. Sexton, K. J. Gregory, L. T. May and A. Christopoulos, *Mol. Pharmacol.*, 2016, **90**, 715–725.
 - 9 L. Aurelio, J.-A. Baltos, L. Ford, A. T. N. Nguyen, M. Jörg, S. M. Devine, C. Valant, P. J. White, A. Christopoulos, L. T. May and P. J. Scammells, *J. Med. Chem.*, 2018, **61**, 2087–2103.
 - 10 A. Glukhova, D. M. Thal, A. T. Nguyen, E. A. Vecchio, M. Jörg, P. J. Scammells, L. T. May, P. M. Sexton and A. Christopoulos, *Cell*, 2017, **168**, 867–877.
 - 11 R. K. Y. Cheng, E. Segala, N. Robertson, F. Deflorian, A. S. Doré, J. C. Errey, C. Fiez-Vandal, F. H. Marshall and R. M. Cooke, *Structure*, 2017, **25**, 1275–1285.
 - 12 C. J. Draper-Joyce, M. Khoshouei, D. M. Thal, Y.-L. Liang, A. T. N. Nguyen, S. G. B. Furness, H. Venugopal, J.-A. Baltos, J. M. Plitzko, R. Danev, W. Baumeister, L. T. May, D. Wootten, P. M. Sexton, A. Glukhova and A. Christopoulos, *Nature*, 2018, **558**, 559–563.
 - 13 R. Franco, S. Ferré, L. Agnati, M. Torvinen, S. Ginés, J. Hillion, V. Casadó, P.-M. Lledó, M. Zoli, C. Lluis and K. Fuxé, *Neuropsychopharmacology*, 2000, **23**, S50–S59.
 - 14 J. P. Pin, T. Galvez and L. Prezeau, *Pharmacol. Ther.*, 2003, **98**, 325–354.
 - 15 Y. Han, I. S. Moreira, E. Urizar, H. Weinstein and J. A. Javitch, *Nat. Chem. Biol.*, 2009, **5**, 688–695.
 - 16 X.-Y. Meng, M. Mezei and M. Cui, *Curr. Pharm. Biotechnol.*, 2014, **15**, 996–1006.
 - 17 S. Marsango, M. J. Varela and G. Milligan, *Methods Mol. Biol.*, 2015, **1335**, 95–105.
 - 18 F. Ciruela, V. Casadó, J. Mallol, E. I. Canela, C. Lluis and R. Franco, *J. Neurosci. Res.*, 1995, **42**, 818–828.
 - 19 E. Gracia, E. Moreno, A. Cortés, C. Lluís, J. Mallol, P. J. McCormick, E. I. Canela and V. Casadó, *Neuropharmacology*, 2013, **71**, 56–69.
 - 20 M. Karplus and J. A. McCammon, *Nat. Struct. Biol.*, 2002, **9**, 646–652.
 - 21 R. O. Dror, A. C. Pan, D. H. Arlow, D. W. Borhani, P. Maragakis, Y. Shan, H. Xu and D. E. Shaw, *Proc. Natl. Acad. Sci. U. S. A.*, 2011, **108**, 13118–13123.
 - 22 A. C. Kruse, J. Hu, A. C. Pan, D. H. Arlow, D. M. Rosenbaum, E. Rosemond, H. F. Green, T. Liu, P. S. Chae, R. O. Dror, D. E. Shaw, W. I. Weis, J. Wess and B. K. Kobilka, *Nature*, 2012, **482**, 552–556.
 - 23 K. J. Kohlhoff, D. Shukla, M. Lawrenz, G. R. Bowman, D. E. Konerding, D. Belov, R. B. Altman and V. S. Pande, *Nat. Chem.*, 2014, **6**, 15–21.
 - 24 Q. Bai, H. Perez-Sanchez, Y. Zhang, Y. Shao, D. Shi, H. Liu and X. Yao, *Phys. Chem. Chem. Phys.*, 2014, **16**, 15874–15885.
 - 25 N. Vaidehi, S. Bhattacharya and A. B. Larsen, in *G Protein-Coupled Receptors – Modeling and Simulation*, ed. M. Filizola, Springer, New York, 2014, pp. 37–54.
 - 26 Y. Li, J. Sun, D. Li and J. Lin, *Phys. Chem. Chem. Phys.*, 2016, **18**, 12642–12650.
 - 27 S. Yuan, H. C. S. Chan, H. Vogel, S. Filipek, R. C. Stevens and K. Palczewski, *Angew. Chem., Int. Ed.*, 2016, **55**, 10331–10335.
 - 28 H. Zhang, G. W. Han, A. Batyuk, A. Ishchenko, K. L. White, N. Patel, A. Sadybekov, B. Zamlynny, M. T. Rudd, K. Hollenstein, A. Tolstikova, T. A. White, M. S. Hunter, U. Weierstall, W. Liu, K. Babaoglu, E. L. Moore, R. D. Katz, J. M. Shipman, M. Garcia-Calvo, S. Sharma, P. Sheth, S. M. Soisson, R. C. Stevens, V. Katritch and V. Cherezov, *Nature*, 2017, **544**, 327–332.
 - 29 A. Bruno, A. E. Guadix and G. Costantino, *J. Chem. Inf. Model.*, 2009, **49**, 1602–1616.
 - 30 M. Neri, S. Vanni, I. Tavernelli and U. Rothlisberger, *Biochemistry*, 2010, **49**, 4827–4832.
 - 31 A. Bruno, C. Beato and G. Costantino, *Future Med. Chem.*, 2011, **3**, 665–681.
 - 32 Q. Bai and X. Yao, *Sci. Rep.*, 2016, **6**, 21763.
 - 33 X. Zhang, Y. Yuan, L. Wang, Y. Guo, M. Li, C. Li and X. Pu, *Phys. Chem. Chem. Phys.*, 2018, **20**, 13485–13496.
 - 34 L. Wang, Y. Yuan, X. Chen, J. Chen, Y. Guo, M. Li, C. Li and X. Pu, *Phys. Chem. Chem. Phys.*, 2018, **20**, 29969–29982.
 - 35 J.-P. Vilardaga, M. Bunemann, C. Krasel, M. Castro and M. J. Lohse, *Nat. Biotechnol.*, 2003, **21**, 807–812.
 - 36 C. Abrams and G. Bussi, *Entropy*, 2014, **16**, 163–199.
 - 37 V. Spiwok, Z. Sucur and P. Hosek, *Biotechnol. Adv.*, 2015, **33**, 1130–1140.
 - 38 Y. Q. Gao, L. Yang, Y. Fan and Q. Shao, *Int. Rev. Phys. Chem.*, 2008, **27**, 201–227.
 - 39 Y. Miao, V. A. Feher and J. A. McCammon, *J. Chem. Theory Comput.*, 2015, **11**, 3584–3595.
 - 40 Y. Miao and J. A. McCammon, *Annu. Rep. Comput. Chem.*, 2017, **13**, 231–278.
 - 41 Y. Miao, A. Bhattachari, A. T. N. Nguyen, A. Christopoulos and L. T. May, *Sci. Rep.*, 2018, **8**, 16836.
 - 42 Y. Miao and J. A. McCammon, *Curr. Opin. Struct. Biol.*, 2016, **41**, 83–89.
 - 43 J. Yang, R. Yan, A. Roy, D. Xu, J. Poisson and Y. Zhang, *Nat. Methods*, 2015, **12**, 7–8.
 - 44 R. Anandakrishnan, B. Aguilar and A. V. Onufriev, *Nucleic Acids Res.*, 2012, **40**, W537–W541.
 - 45 D. A. Case, I. Y. Ben-Shalom, S. R. Brozell, D. S. Cerutti, T. E. Cheatham, III, V. W. D. Cruzeiro, T. A. Darden, R. E. Duke, D. Ghoreishi, M. K. Gilson, H. Gohlke,

- A. W. Goetz, D. Greene, R. Harris, N. Homeyer, S. Izadi, A. Kovalenko, T. Kurtzman, T. S. Lee, S. LeGrand, P. Li, C. Lin, J. Liu, T. Luchko, R. Luo, D. J. Mermelstein, K. M. Merz, Y. Miao, G. Monard, C. Nguyen, H. Nguyen, I. Omelyan, A. Onufriev, F. Pan, R. Qi, D. R. Roe, A. Roitberg, C. Sagué, S. Schott-Verdugo, J. Shen, C. L. Simmerling, J. Smith, R. Salomon-Ferrer, J. Swails, R. C. Walker, J. Wang, H. Wei, R. M. Wolf, X. Wu, L. Xiao, D. M. York and P. A. Kollman, *AMBER 2018*, University of California, San Francisco, 2018.
- 46 G. M. Morris, R. Huey, W. Lindstrom, M. F. Sanner, R. K. Belew, D. S. Goodsell and A. J. Olson, *J. Comput. Chem.*, 2009, **30**, 2785–2791.
- 47 G. Lebon, T. Warne, P. C. Edwards, K. Bennett, C. J. Langmead, A. G. W. Leslie and C. G. Tate, *Nature*, 2011, **474**, 521–525.
- 48 J. Kim, J. Wess, A. M. van Rhee, T. Schoneberg and K. A. Jacobson, *J. Biol. Chem.*, 1995, **270**, 13987–13997.
- 49 W. L. Jorgensen, J. Chandrasekhar, J. D. Madura, R. W. Impey and M. L. Klein, *J. Chem. Phys.*, 1983, **79**, 926–935.
- 50 J. A. Maier, C. Martinez, K. Kasavajhala, L. Wickstrom, K. E. Hauser and C. Simmerling, *J. Chem. Theory Comput.*, 2015, **11**, 3696–3713.
- 51 J. Wang, R. M. Wolf, J. W. Caldwell, P. A. Kollman and D. A. Case, *J. Comput. Chem.*, 2004, **25**, 1157–1174.
- 52 C. J. Dickson, B. D. Madej, A. A. Skjervik, R. M. Betz, K. Teigen, I. R. Gould and R. C. Walker, *J. Chem. Theory Comput.*, 2014, **10**, 865–879.
- 53 R. W. Pastor, B. R. Brooks and A. Szabo, *Mol. Phys.*, 1988, **65**, 1409–1419.
- 54 J.-P. Ryckaert, G. Ciccotti and H. J. C. Berendsen, *J. Comput. Phys.*, 1977, **23**, 327–341.
- 55 T. Darden, D. York and L. Pedersen, *J. Chem. Phys.*, 1993, **98**, 10089–10092.
- 56 A. Barducci, G. Bussi and M. Parrinello, *Phys. Rev. Lett.*, 2008, **100**, 020603.
- 57 M. Bonomi, D. Branduardi, G. Bussi, C. Camilloni, D. Provasi, P. Raiteri, D. Donadio, F. Marinelli, F. Pietrucci, R. A. Broglia and M. Parrinello, *Comput. Phys. Commun.*, 2009, **180**, 1961–1972.
- 58 Y. Miao and J. A. McCammon, *Annu. Rep. Comput. Chem.*, 2017, **13**, 231–278.
- 59 W. Humphrey, A. Dalke and K. Schulten, *J. Mol. Graphics Modell.*, 1996, **14**, 33–38.
- 60 D. R. Roe and T. E. Cheatham, III, *J. Chem. Theory Comput.*, 2013, **9**, 3084–3095.
- 61 Y. Miao, W. Sinko, L. Pierce, D. Bucher, R. C. Walker and J. A. McCammon, *J. Chem. Theory Comput.*, 2014, **10**, 2677–2689.
- 62 J. Eargle and Z. Luthey-Schulten, *Bioinformatics*, 2012, **28**, 3000–3001.
- 63 A. Sethi, J. Eargle, A. A. Black and Z. Luthey-Schulten, *Proc. Natl. Acad. Sci. U. S. A.*, 2009, **106**, 6620–6625.
- 64 N. M. Glykos, *J. Comput. Chem.*, 2006, **27**, 1765–1768.
- 65 J. Duch and A. Arenas, *Phys. Rev. E: Stat., Nonlinear, Soft Matter Phys.*, 2005, **72**, 027104.
- 66 A. Kourounakis, C. Visser, M. de Groot and A. P. Ijzerman, *Biochem. Pharmacol.*, 2001, **61**, 137–144.
- 67 B. G. Tehan, A. Bortolato, F. E. Blaney, M. P. Weir and J. S. Mason, *Pharmacol. Ther.*, 2014, **143**, 51–60.
- 68 G. E. Rovati, V. Capra and R. Neubig, *Mol. Pharmacol.*, 2007, **71**, 959–964.
- 69 L. Ye, N. Van Eps, M. Zimmer, O. P. Ernst and R. Scott Prosser, *Nature*, 2016, **533**, 265–268.
- 70 S. Vohra, B. Taddese, A. C. Conner, D. R. Poyner, D. L. Hay, J. Barwell, P. J. Reeves, G. J. Upton and C. A. Reynolds, *J. R. Soc., Interface*, 2013, **10**, 20120846.
- 71 N. Sartania, S. Appelbe, J. D. Pediani and G. Milligan, *Cell. Signalling*, 2007, **19**, 1928–1938.
- 72 D. El Moustaine, S. Granier, E. Doumazane, P. Scholler, R. Rahmeh, P. Bron, B. Mouillac, J. L. Baneres, P. Rondard and J. P. Pin, *Proc. Natl. Acad. Sci. U. S. A.*, 2012, **109**, 16342–16347.
- 73 W. Guo, L. Shi, M. Filizola, H. Weinstein and J. A. Javitch, *Proc. Natl. Acad. Sci. U. S. A.*, 2005, **102**, 17495–17500.
- 74 B. Jastrzebska, D. Fotiadis, G. F. Jang, R. E. Stenkamp, A. Engel and K. Palczewski, *J. Biol. Chem.*, 2006, **281**, 11917–11922.
- 75 J. Petersen, S. C. Wright, D. Rodriguez, P. Matricon, N. Lahav, A. Vromen, A. Friedler, J. Stromqvist, S. Wennmalm, J. Carlsson and G. Schulte, *Nat. Commun.*, 2017, **8**, 226.
- 76 J. M. Johnston, H. Wang, D. Provasi and M. Filizola, *PLoS Comput. Biol.*, 2012, **8**, e1002649.